ADVANCED
MATERIALS
www.advmat.de

Materials Views
www.MaterialsViews.com

COMMUNICATION

Nanoparticle-Loaded Protein–Polymer Nanodroplets for Improved Stability and Conversion Efficiency in Ultrasound Imaging and Drug Delivery

Jeong Yu Lee, Dario Carugo, Calum Crake, Joshua Owen, Marie de Saint Victor, Anjali Seth, Constantin Coussios, and Eleanor Stride*

Ultrasound is one of the most widely applied clinical imaging modalities on account of its ability to provide real time images particularly of blood flow, its cost effectiveness, and high patient acceptability.[1–3] Over the past two decades, research into the therapeutic applications of ultrasound has also expanded significantly for indications ranging from cancer therapy to thrombolysis.[4] An important area has been the development of gas-filled microbubbles both as image contrast agents and more recently as a means of enhancing therapeutic delivery.[5] Of particular interest is the fact that numerous studies have shown that microbubbles can facilitate the intracellular delivery of molecules under ultrasound exposure.[6]

Over the last decade there has been increasing interest in the use of liquid perfluorocarbon (PFC) droplets as alternatives to microbubbles.[7] It has been shown that nanoscale droplets of appropriate size are able to pass through the endothelial gaps of defective blood vessels surrounding tumours, thus addressing the disadvantages of microbubbles, such as poor stability and micrometer size.[8,9] By selecting PFC liquids with the appropriate properties, nanodroplets can be fabricated so that they will undergo a phase transition upon exposure to ultrasound of sufficient intensity and/or a temperature increase from another source. The resulting gas/vapour bubble can then be utilized for vascular imaging and/or therapeutic delivery either to promote drug uptake[2,10] or, e.g., for vessel occlusion, molecular recognition in cancer detection, or ablation for cancer therapy.[8,11]

Notwithstanding their significant potential, the development of nanodroplets still poses some considerable challenges. While nanodroplet stability is greatly enhanced compared with that of microbubbles, it is still relatively poor compared with that of solid particles,[3] and droplets may undergo coalescence and/or premature phase transition before they reach the target region. Once in the target region, the conversion efficiency, i.e., the proportion of droplets undergoing a phase change for a given set of ultrasound exposure conditions is also often very low.[12] Prior to conversion, nanodroplets cannot be continuously imaged under ultrasound and most current formulations rely on passive targeting, e.g., by the enhanced permeability and retention (EPR) effect.

In this study we examined potential solutions to these challenges. First, we investigated a hybrid protein–polymer shell for coating the nanodroplets consisting of human serum albumin (HSA) and poly(ethylene glycol) (PEG) (**Figure 1**) with the aim of improving stability. Albumin coatings are widely used in particle formulations as they offer excellent biocompatibility and desirable surface properties. The binding affinity for hydrophobic molecules is however limited and this limits the stability of albumin coated particles and hence their circulation time. Previous work[13] has indicated that cross-linking of the albumin using a polymer can generate extremely stable structures and our aim was to see whether this approach could be used to improve nanodroplet stability. Other studies have also shown that oleic acid-functionalized iron oxide nanocrystals (IONCs) can be very effectively stabilized with an aqueous dodecyltrimethylammonium bromide (DTAB) solution due to the hydrophobic van der Waals interaction between the oleic acid of IONCs and the hydrocarbon chains of DTAB.[14] We therefore also prepared nanodroplets containing PFC and IONCs coated with DTAB for comparison (**Table 1**).

Second, we investigated the effect of loading the nanodroplets with superparamagnetic solid nanoparticles to act as nucleation agents to promote phase transition thereby improving conversion efficiency. The particles also potentially provide a means of manipulating the droplets using an external magnetic field which has been shown in previous work to be highly advantageous for drug delivery.[10d] We first determined the effect upon the physical properties of the nanodroplets in terms of their size, surface charge, and stability under physiological conditions. Their response to ultrasound exposure was then examined to determine conversion efficiency, change in size and potential for image contrast enhancement.

Finally the ability of the nanodroplets to encapsulate, release, and promote uptake of a drug in a cancer cell line was tested. Albumin–PEG hybrid nanoparticles encapsulating superparamagnetic iron oxide and a hydrophobic drug (Paclitaxel) were prepared using an oil-in-water emulsification method. These intermediate nanoparticles (mHSA) had an average diameter of 232.0 ± 12.3 nm as measured by dynamic light scattering (DLS). Following perfluoropentane (PFP) loading, the

Dr. J. Y. Lee, Dr. D. Carugo, C. Crake, Dr. J. Owen,
M. de Saint Victor, Dr. A. Seth, Prof. C. Coussios,
Prof. E. Stride
Institute of Biomedical Engineering
Department of Engineering Science
Old Road Campus Research Building
University of Oxford
Oxford OX3 7DQ, UK
E-mail: eleanor.stride@eng.ox.ac.uk

Materials
Views
www.MaterialsViews.com

ADVANCED
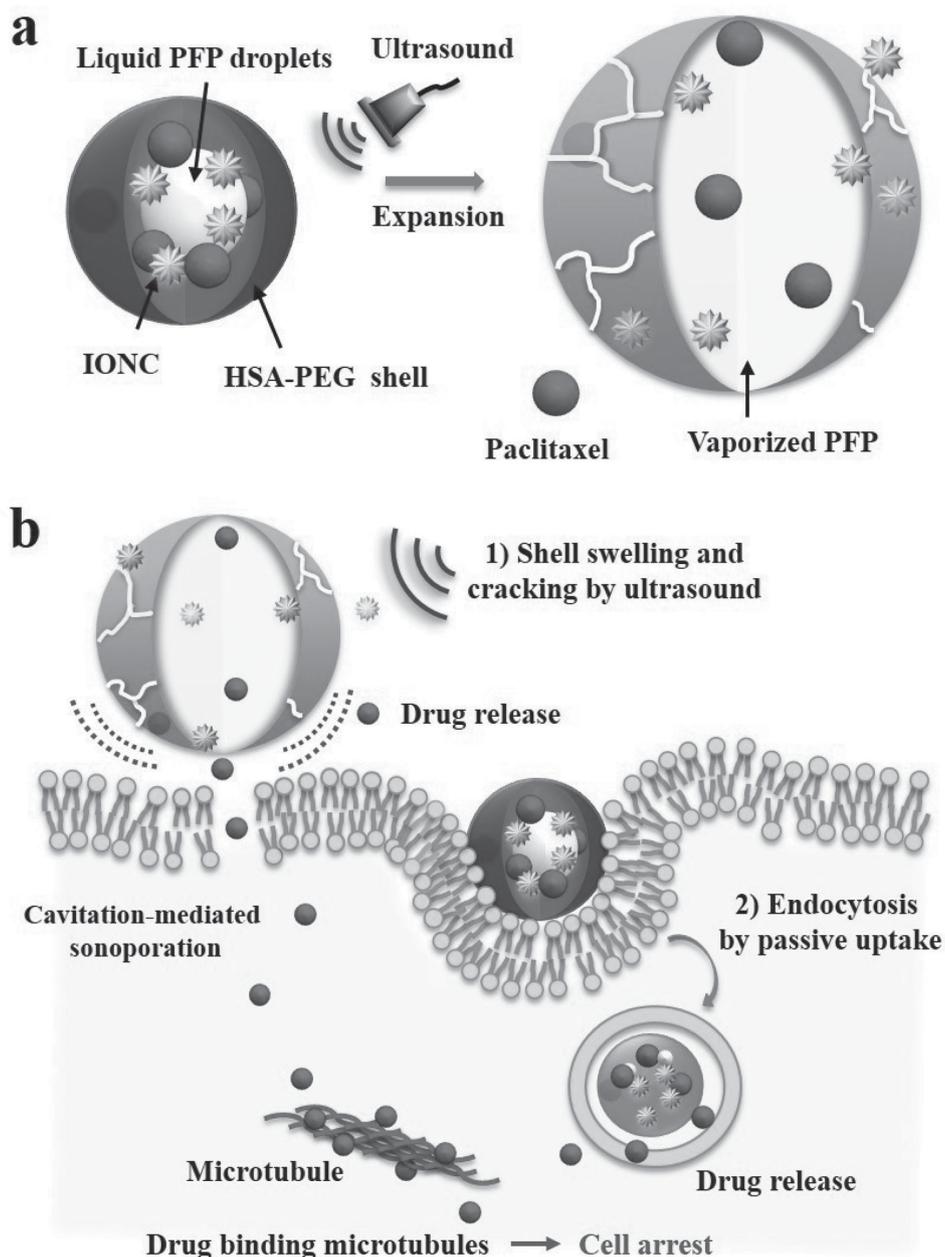MATERIALS
www.advmat.de

COMMUNICATION

Figure 1. a) Schematic representation of protein–polymer hybrid nanodroplets incorporating iron oxide nanocrystals, hydrophobic drugs, and perfluoropentane. As the liquid PFP is vaporized upon ultrasound exposure, microscale bubbles are formed. This process also promotes the release of the encapsulated drugs through compromised areas of the protein–polymer coating. b) Different pathways of drug release and intracellular uptake: (1) after ultrasound exposure, drugs may be taken up by passive diffusion and sonoporation; (2) by endocytosis, droplets are degraded in the lysosomes, which facilitates drug release inside the cell.

size of the nanodroplets (mHSA-PFP) was measured again and found to be 351.4 ± 18.5 nm and 416.2 ± 25.4 nm at 20 °C and 37 °C, respectively. The latter measurement was made to determine whether there would be any change in vivo (**Figure 2**a).

Earlier studies using the Antoine vapour pressure equation have shown that the estimated vaporization temperature of a PFP droplet should increase geometrically as the droplet size decreases into the sub-micrometer range.[15] Therefore

nanodroplets containing liquid PFP should be stable at physiological temperatures, notwithstanding variations in surface tension produced by materials at the droplet surface.[16] This was found to be true for the mHSA-PFP droplets (Figure S1, Supporting Information) and should allow the particles to remain as droplets in the circulation rather than convert to microbubbles at 37 °C (i.e., following injection into the body) and subsequently to extravasate into tumours. The average size of the magnetic particle-loaded

Table 1. Formulations of nanodroplets and nanoparticles used in the experiments.

Materials\nanodroplets		HSA-PFP	mHSA-PFP	mpHSA-PFP	mpHSA	mDTAB-PFP
Core	Magnetic particles (Fe₃O₄, 5 nm)	0	500 μg	500 μg	500 μg	500 μg
	Paclitaxel (PTX)	0	0	500 μg	500 μg	0
	Perfluoropentane (PFP)	50 μL	50 μL	50 μL	0	50 μL
Shell	Human serum albumin (HSA)	4 mg	4 mg	4 mg	4 mg	0
	bis-NHS-PEG	6 mg	6 mg	6 mg	6 mg	0
	Dodecyltrimethyl-ammonium bromide (DTAB)	0	0	0	0	30×10^{-3} M

DTAB nanodroplets (mDTAB-PFP) however increased from 422 ± 24 nm at 20 °C to 1058 ± 53 nm at 37 °C. This may be attributed to aggregation of the droplets due to the relatively poor stabilization provided by the DTAB coating resulting in a lower vaporization temperature than would be predicted from the size distribution at 20 °C.

Transmission electron microscopy (TEM) was performed to confirm the size and structure of both mHSA-PFP and mDTAB-PFP (Figure 2b and Figure S1, Supporting Information). It was not possible to directly observe the PFP liquid core under vacuum. However, the remaining hollow space inside the droplets was observed after gentle drying of the sample on the carbon grid.

Changes in the concentration of nanodroplets between 200 and 800 nm were measured using the Nanosight system at 37 °C over a period of 10 d (Figure 2c). The concentration of mDTAB-PFP decreased rapidly at 37 °C. Within 6 h, 49% of mDTAB-PFP were lost and only 7.2% remained after 10 d. However, the concentration of mHSA-PFP reduced by just 3.5% in the first 6 h, and 76% of nanodroplets were still detectable after 10 d.

Macroscopic observation of vials of droplets stored at 37 °C also indicated that mHSA-PFP droplets were significantly more stable than mDTAB-PFP (Figure S3, Supporting Information). Similarly, in the case of the paclitaxel-loaded nanodroplets, 82% of the initial concentration was detectable after 15 d and could still be readily vaporized upon ultrasound exposure (Figure S4, Supporting Information). These data indicate the stability of the HSA-PFP nanodroplets at in vivo temperatures, and, as shown in previous studies[7] this suggests that the cross linked albumin coating was able to increase the vaporization temperature of the PFP droplets significantly above the bulk liquid boiling point of 29 °C (Figure S1, Supporting Information). This stability may have been further augmented by disulfide bonds between cysteine residues formed during sonication.[17] Interestingly, the presence of magnetic nanoparticles also improved stability. This could perhaps be attributed to a form of Pickering stabilization, i.e., the solid hydrophobic particles accumulate at the interface of the perfluorocarbon core (see Figure S2, Supporting Information) from which they are excluded on account of its combination of hydrophobicity and lipophobicity. The resulting surface layer then prevents both diffusion of the PFP or droplet coalescence.[18]

Using the experimental setup described in Figure S5 (Supporting Information), nanodroplets were converted into microbubbles under the action of continuous wave (CW) ultrasound. The experimentally measured resonant frequency and fixed peak-to-peak voltage for the device were ≈1.85 MHz and 40 V, respectively. In addition, the resulting peak rarefactional pressure in the chamber was 265 kPa. Bright-field optical microscopy images of mHSA-PFP, HSA-PFP, and mDTAB-PFP suspended in pig plasma were captured before and after either 15 or 45 s of CW ultrasound exposure (**Figure 3**a). The highest concentration of microbubbles was generated by the mHSA-PFP droplets after 45 s. Equivalent ultrasound images are shown in Figure S6 in the Supporting Information. The changes in size distribution and concentration were quantified using the Nanosight system (Figure 3b). The initial concentration of mHSA-PFP droplets was 6.2×10^8 particles mL^{-1} before ultrasound exposure. After 15 s of continuous ultrasound exposure a dramatic decrease in the population of nanodroplets to 56% was observed, decreasing further to 29% after 45 s; i.e., ≈70% of the droplets responded to ultrasound and underwent a phase change. The results for longer exposure times are shown in Figure S7 in the Supporting Information together with scanning electron micrographs of droplets following ultrasound exposure (Figure S8, Supporting Information).

In contrast with the mHSA-PFP, the change in the HSA-PFP droplets was less dramatic; after 45 s 75% of the HSA-PFP droplets were still present. This phenomenon could be explained by the magnetic nanoparticles acting as nucleation agents for the vaporization process. This hypothesis is supported by the results of previous studies in which solid particles were shown to reduce the vaporization threshold of nanodroplets (HSA-PFP).[19] Other mechanisms may also be involved in lowering the droplet vaporization pressure threshold: e.g., changes in the acoustic properties of the droplets due to the IONCs could contribute to superharmonic focusing effects which have also been shown to significantly affect vaporization thresholds.[20] Interestingly, phase transition was not so readily observed directly with mDTAB-PFP under the microscope; although the measured extent of the population decrease was 8% higher than that of HSA-PFP after 45 s. This may have been due to rapid dissolution of the resulting microbubbles.

The albumin–PEG conjugate coating appeared to provide stabilization for the microbubbles as well the nanodroplets. In Figure 3c, the histogram of bubble sizes from mHSA-PFP nanodroplets is shown, as determined by direct observation under the optical microscope. The average diameter of the converted bubbles was 8.17 μm, and 64.1% of bubbles formed were smaller than 10 μm. However, the size of the observed microbubbles formed by vaporization was twice as large as that predicted by theoretical approximation calculated using the ideal gas law ($PV = nRT$).[21] When a droplet of PFP (molar mass:
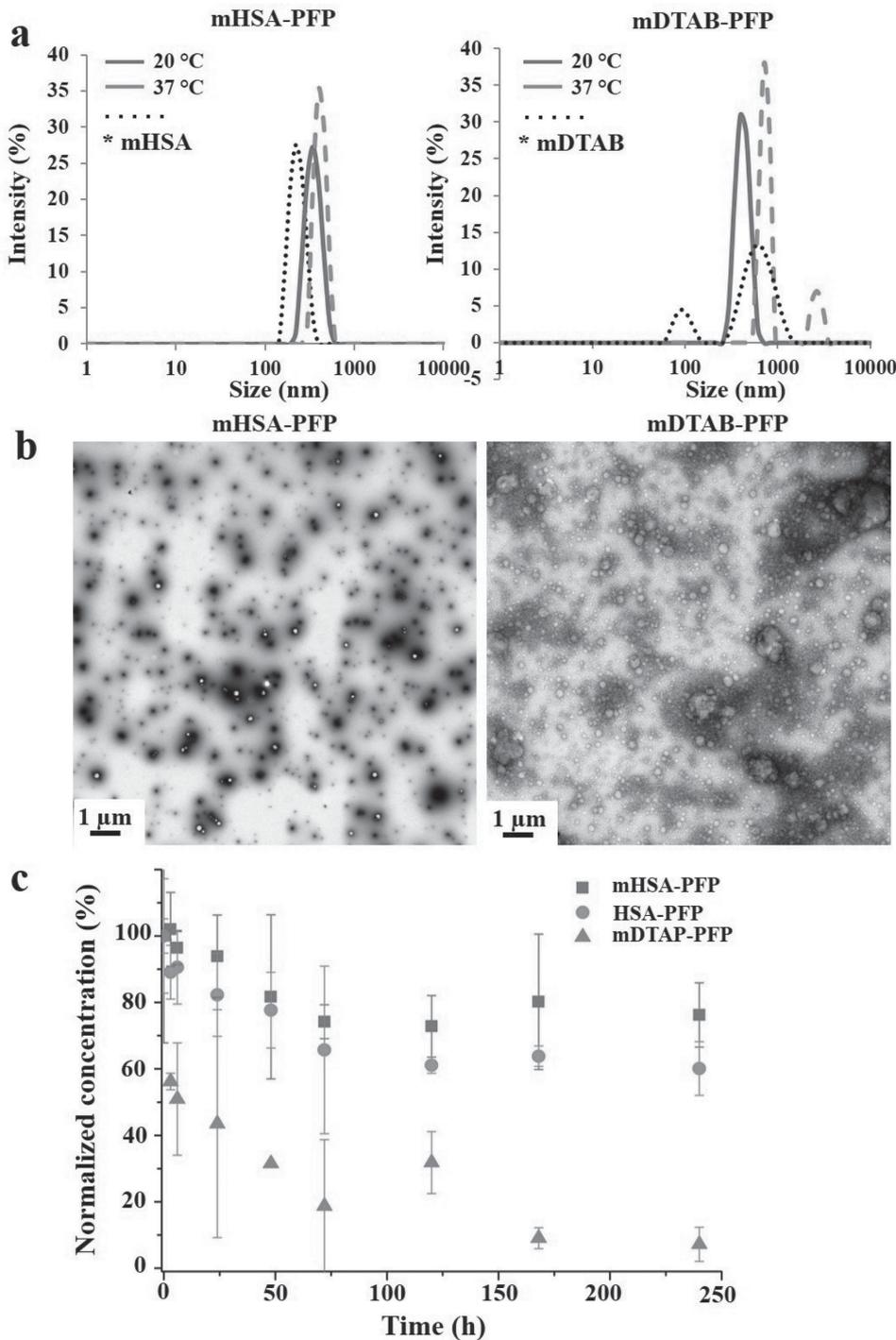
Materials
Views
www.MaterialsViews.com

ADVANCED
MATERIALS
www.advmat.de

COMMUNICATION

Figure 2. a) Hydrodynamic diameters of mHSA-PFP (left) and mDTAB-PFP (right) at 20 °C and 37 °C. b) Transmission electron microscopy (TEM) images of mHSA-PFP and mDTAB-PFP droplets. c) Concentration changes of mHSA-PFP, HSA-PFP, and mDTAB-PFP over time at 37 °C. The initial concentrations of mHSA-PFP, HSA-PFP, and mDTAB-PFP nanodroplets were 4.7×10^9, 4.6×10^9, and 4.1×10^9 particles in mL, respectively.

0.288 kg mol^{-1}) undergoes a phase conversion to the gaseous state at 37 °C, it should expand to maximally 8.9 times its original diameter (neglecting surface tension effects and other deviations from the ideal gas law). This may have been due to coalescence of individual microbubbles in close proximity; or

absorption of dissolved gases from the pig plasma which was not degassed.

Encapsulation of paclitaxel in the nanodroplets was measured by detecting UV absorbance of paclitaxel. The encapsulation efficiency was 93% ± 6% and the maximum payload
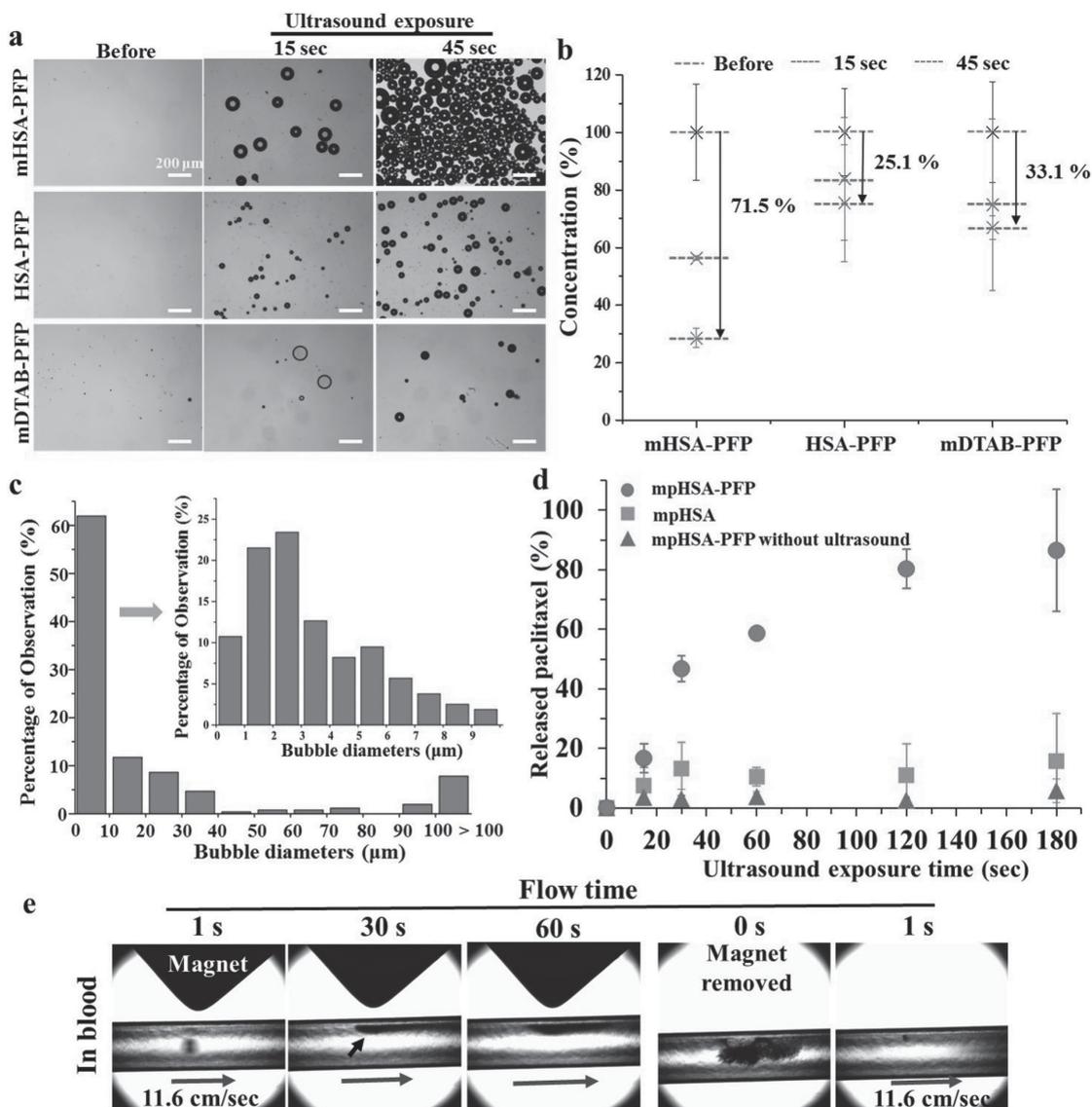
Figure 3. a) Optical images of the mHSA-PFP, HSA-PFP, and mDTAB-PFP nanodroplets before and after 15 or 45 s of ultrasound exposure. Scale bars represent 200 μm. b) Normalized concentration of each nanodroplet before and after ultrasound exposure. The initial concentrations of mHSA-PFP, HSA-PFP, and mDTAB-PFP nanodroplets were 6.2×10^8, 5.2×10^8, and 4.9×10^8 particles per mL, respectively. c) Size distribution of bubbles produced from mHSA-PFP droplets by 1 min of ultrasound exposure. The initial concentration was 2.1×10^8 particles per mL. d) Release profiles of paclitaxel from mpHSA-PFP nanodroplets and mpHSA nanoparticles with varying ultrasound exposure time and mpHSA-PFP without ultrasound exposure. e) Localization, retention, and redispersion of mHSA-PFP nanodroplets in a vessel phantom under the influence of external magnetic field. The short black arrow in the 2nd panel indicates accumulated nanodroplets. The Initial concentration was 3.1×10^8 particles per mL, and mean blood velocity was 11.6 cm s^{-1}.

was about 0.096 mg mL^{-1} for paclitaxel-loaded mHSA-PFP nanodroplets (mpHSA-PFP). The in vitro release behavior of the mpHSA-PFP and paclitaxel-loaded mHSA nanoparticles (mpHSA, the maximum payload: 0.10 mg mL^{-1}) was observed in the ultrasound field (Figure 3d). The release of paclitaxel from mpHSA-PFP was measured over the same time course, without ultrasound exposure. The concentration of released paclitaxel molecules was inferred from the degree of absorbance intensity. Sustained release was found to be dependent upon the ultrasound exposure time. After 1 min of exposure,

59% of the paclitaxel was released from the nanodroplets, and 90% was released within 3 min. Conversely, less than 20% of the paclitaxel was released from mHSA nanoparticles in 3 min. The results indicate that the paclitaxel release of mHSA-PFP was in response to the ultrasound exposure. Furthermore, the release profile is highly interrelated to the droplet-to bubble conversion rate. Unexposed nanodroplets released a negligible quantity of paclitaxel over the same time period.

The aim of magnetically guided drug delivery is to maximize the concentration of functionalized therapeutic agents at

a target site using a magnetic field.[22] Successful magnetic targeting of the nanodroplets was observed in a vessel mimicking phantom in 95% pig blood, as shown in Figure 3e. In this experiment, blood flow was fixed at 11.6 cm s^{-1} which is in the range corresponding to venous flow.[23] In the absence of the magnet, the nanodroplets dispersed in the blood solution passed through the tube (Figure S9, Supporting Information). With the magnet, the mpHSA-PFP was rapidly concentrated at the wall of the tube closest to the magnet (field = 0.4 T). After 1 min, the magnet was removed and the accumulated droplets were carried away with no evidence of aggregation. Thus this method could be used to assist transport of nanodroplets to increase targeting efficiency as compared with that achievable by, e.g., the EPR effect or biochemical targeting; although all three methods could be used in a complementary fashion.

The degree of cancer cell proliferation was determined to evaluate the therapeutic potential of the mpHSA-PFP droplets when they are exposed to ultrasound. Paclitaxel-free nanodroplets (mHSA-PFP) were used as a negative control at the same concentration. In addition paclitaxel-loaded HSA nanoparticles (mpHSA) and free paclitaxel were tested for comparison. Previously, we have developed acoustically and biologically compatible chambers for ultrasound-mediated delivery of therapeutic compounds to cancer cells.[24] A schematic of the set-up is illustrated in **Figure 4**a. Samples were added to the media of Michigan Cancer Foundation (MCF) 7 cells shortly before loading the chamber into the ultrasound set-up. As shown in Figure 4b, there was no significant effect of free paclitaxel with ultrasound. On the other hand, paclitaxel in nanocarriers with ultrasound effectively inhibited the growth of cancer cells in a synergistic manner. With ultrasound exposure, mpHSA-PFP exhibited a reduction in cell viability of 45.7% ± 4.62% after 24 h of incubation, whereas mpHSA decreased the cell viability to a smaller extent (14.5% ± 3.54%) at an equivalent concentration of paclitaxel (80 × 10^{-9} M). Acoustic droplet vaporization has been shown previously to induce cell membrane permeabilization.[25] In addition, rapidly expanding bubbles may increase contact between cell membranes and drugs, resulting in increased uptake of paclitaxel. Furthermore, mHSA-PFP also showed a small degree of cytotoxicity to the cancer cells in the ultrasound field. Oscillating bubbles and or the fluid motion induced by the process (microstreaming) could stretch and tear the membranes of nearby cells.[26,27] This mechanical force would initiate the cell swelling, cytolysis, and eventually death.[26]

During ultrasound exposure, the phase transition was monitored using passive acoustic mapping (PAM) (Figure 4c–h).[28] The evolution of cavitation activity was measured over time expressed as the maximum cavitation power from each frame of PAM data and the averaged spectra for the emissions from the focal point were also calculated in each experiment after reconstruction. As shown in Figure 4c, the annotated B-mode image as seen by the monitoring probe shows the sample holder when the focus of the HIFU transducer is in the centre of the image. In the absence of particles or nanodroplets the energy distribution was approximately uniform (max. value 91.86 energy units) and represents the baseline signal level for the system due to background cavitation of the media, reflections from the magnet, and electrical noise. As a result the time trace

and spectra within the frequency range of the probe were both approximately flat (Figure 4g,h, blue lines). When the cells were treated with mpHSA nanoparticles not containing PFP, a small increase in the PAM signal was observed. Consequently, the map was no longer uniform, with a small peak visible toward the location of the HIFU focus (max. value 100.06 energy units) (Figure 4e). The corresponding time trace (Figure 4g, green line) showed that this was primarily due to increased cavitation in the first frame of ultrasound data. Finally, with mpHSA-PFP nanodroplets a more pronounced increase in cavitation energy was observed (max. value 140.68 energy units), which was maintained above baseline for the duration of the monitoring period (Figure 4g, red line). The corresponding spectra (Figure 4h, red line) showed the pronounced harmonic and ultraharmonic peaks suggestive of noninertial cavitation, as well as an increase in the broadband signal level associated with inertial cavitation.[29] These results imply that these ultrasound conditions were sufficient to trigger vaporization of the nanodroplets into bubbles whose acoustic response was sufficient for them to be observed using PAM.

To determine the main effects on the cancer cells, their size and shape were observed using an optical microscope, and propidium iodide (PI) was used to stain the nuclear DNA contents of each group (**Figure 5**). During apoptosis, active biochemical events occur in the cells and consequentially induce morphological changes in the cell and DNA cleavage.[30] The optical images showed changes in cell morphology after treatment with the drug/droplets and ultrasound exposure, especially with mpHSA-PFP. The cell population was clearly reduced as shown in the images, also the morphology was changed on account of paclitaxel-induced apoptosis. Cell shrinkage and blebbing, typical of cell apoptosis,[31] were observed with mpHSA-PFP. Similar cell shrinkage was observed with mpHSA nanoparticles. Interestingly, with mHSA-PFP, blebby cells with debris were occasionally observed perhaps because microbubbles created from nanodroplets damaged cells. Cells undergoing apoptosis could be identified as a population with diminished DNA content shown as an accumulated sub G1 population. Cells treated with both mHSA-PFP and mpHSA showed a relatively high percentage of sub G1 population of 11.6% and 11%, respectively, compared to cells only. The MCF-7 cells treated with mpHSA-PFP showed 26.4% of sub G1 cell fraction while 6.31% of cells was presented in the same phase in the free paclitaxel sample. The mpHSA-PFP enhanced not only the extent but also the rate of apoptosis-inducing cell death. Paclitaxel has antimitotic activity by preventing polymerization of tubulin polymers during replication in the late G2/M phase of the cell cycle, and the arrest in G2/M phase leads to cell death through an apoptotic mechanism.[32] The cells with mpHSA showed relatively high cell population at this stage due to the paclitaxel working mechanism. Compared to mpHSA, mpHSA-PFP exhibited a lower percentage of cells at the G2/M stage because cells had already undergone the process of cell death. This is likely due to the synergistic effect of chemotherapy (paclitaxel) and physical effect of PFP vaporization.

In summary, we have developed a novel protein–polymer coated nanodroplet as an ultrasound-triggered imaging and therapeutic agent. This type of nanodroplet was demonstrated to be stable at body temperature over 10 d and highly responsive
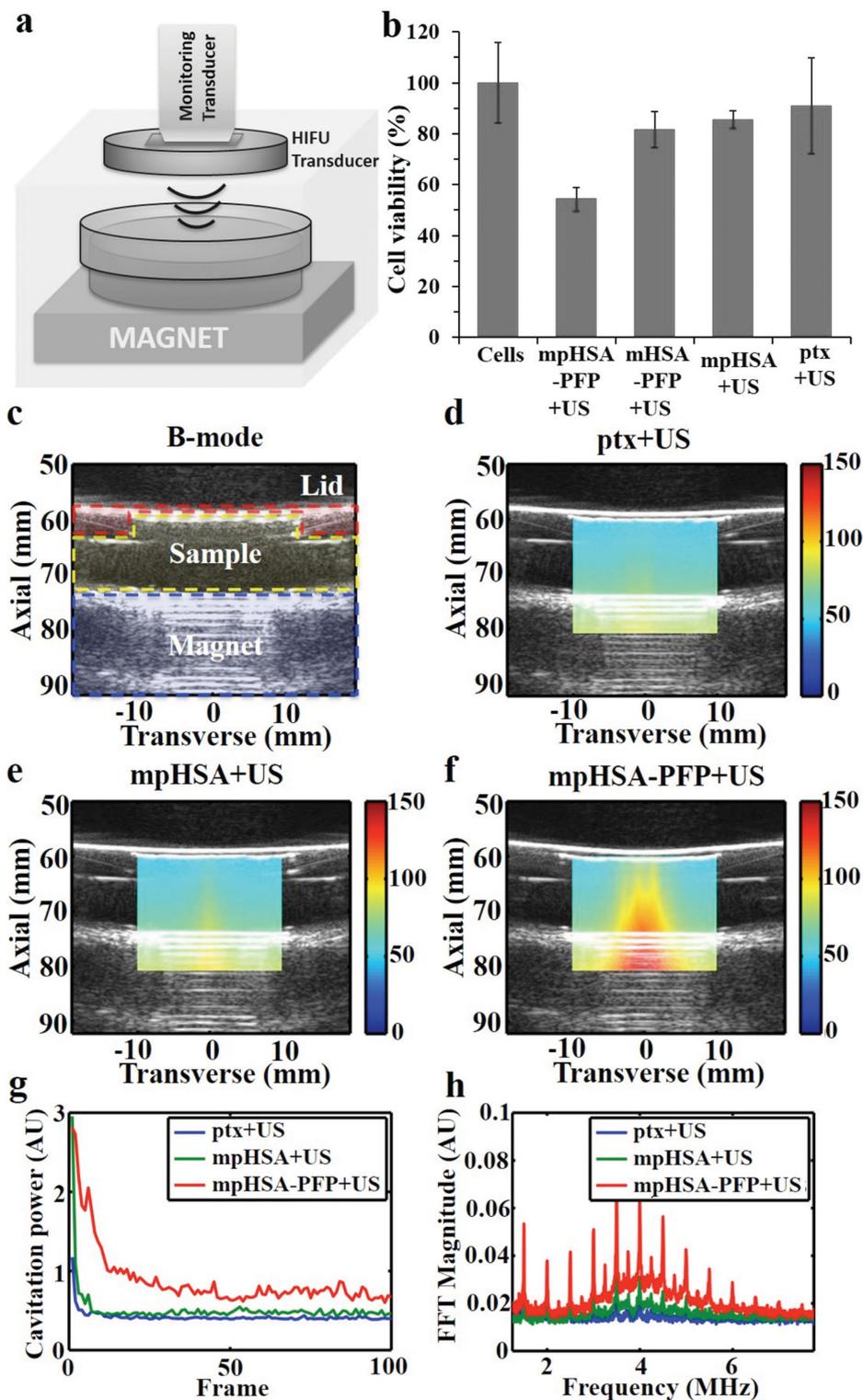
Figure 4. a) Schematic illustration of instrumental setup for ultrasound-mediated intracellular delivery of paclitaxel. b) The viability of cells incubated for 24 h following treatment with ultrasound and: medium, mpHSA-PFP, mHSA-PFP, mpHSA or free paclitaxel, at an equivalent drug concentration of 1 µg mL^{-1}. c) Annotated B-mode image showing the sample chamber, magnet, and lid as seen from the imaging array. Axes are defined relative to the centre of the front face of the imaging array. d–f) Pre-exposure B-mode images with PAM overlay showing sum of all frames for each exposure for paclitaxel only (d), paclitaxel + nanoparticles (e), and paclitaxel + nanodroplets (f). Colour bars represent total cavitation energy (AU). g,h) Evolution of cavitation activity over time and spectra for the first exposure from each sample. g) Maximum cavitation power (AU) from each frame of PAM data. g) Fast Fourier transform (FFT) magnitude (AU) of the reconstructed PAM signal from the focal point.
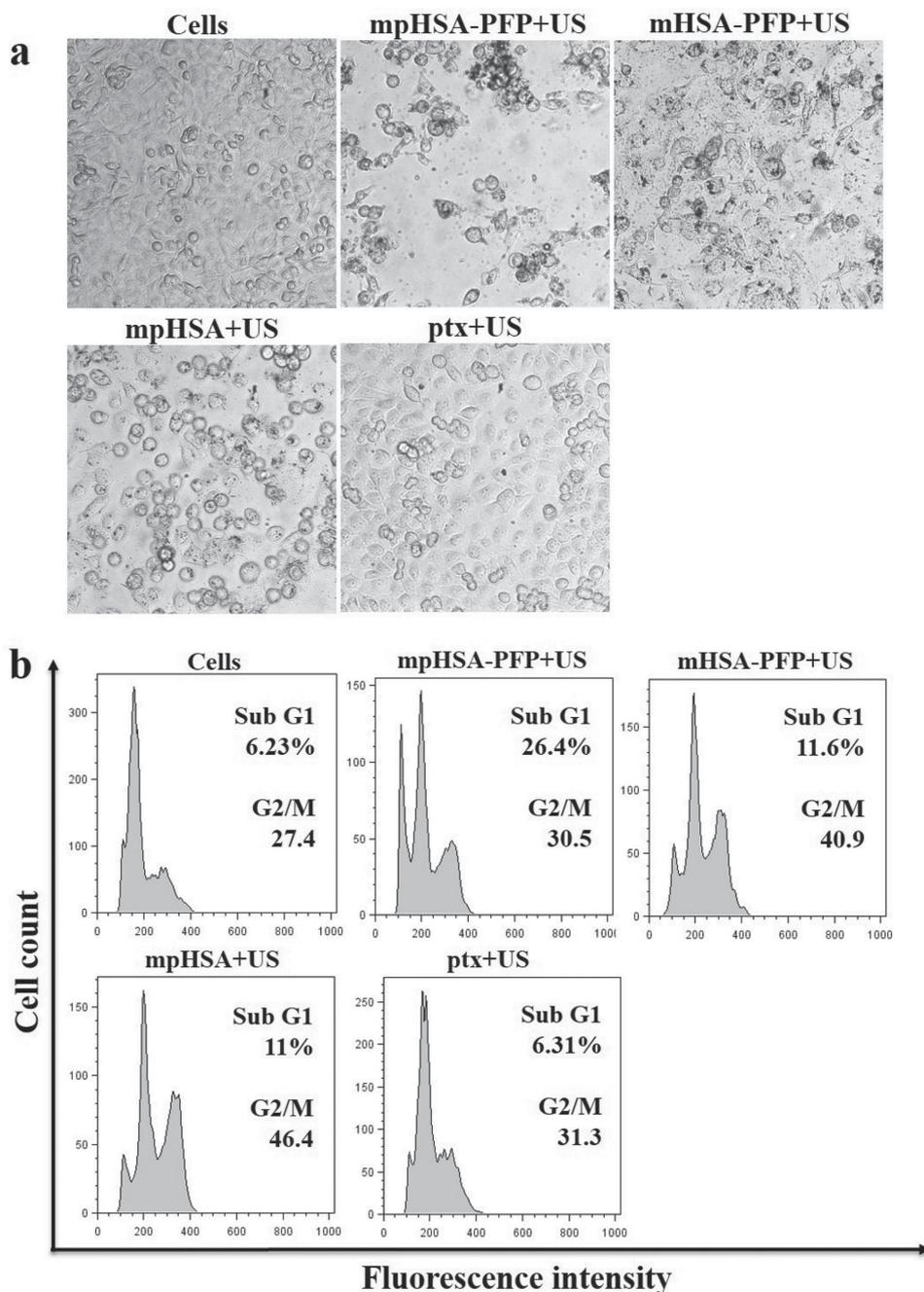
Figure 5. a) Bright-field images and b) flow cytometric analysis of the cell cycles of MCF-7 cells incubated with mpHSA-PFP, mHSA-PFP, mpHSA and free paclitaxel for 24 h after applied ultrasound at an equivalent drug concentration of 1 µg mL^{-1}.

to ultrasound stimulus. These protein–polymer nanodroplets showed excellent stability at in vivo temperatures and over prolonged time periods, as compared with single-chain surfactant coated nanodroplets. The nanodroplet formulation also contains IONCs that make the droplets both magnetically responsive and greatly improve droplet:bubble conversion efficiency upon ultrasound exposure. Finally, we have demonstrated the efficacy of the nanodroplets for the delivery of paclitaxel to cancer cells in an in vitro model.

Supporting Information

Supporting Information is available from the Wiley Online Library or from the author.

Acknowledgements

[1] a) C. J. Harvey, J. M. Pilcher, R. J. Eckersley, M. J. Blomley, D. O. Cosgrove, *Clinical Radiol.* **2002**, *57*, 157; b) M. A. Nakatsuka, M. J. Hsu, S. C. Esener, J. N. Cha, A. P. Goodwin, *Adv. Mater.* **2011**, *23*, 4908.

[2] N. Rapoport, *Wiley Interdisciplinary Rev. Nanomed. Nanobiotechnol.* **2012**, *4*, 492.

[3] H. S. Min, S. Son, T. W. Lee, H. Koo, H. Y. Yoon, J. H. Na, Y. Choi, J. H. Park, J. Lee, M. H. Han, R. W. Park, I. S. Kim, S. Y. Jeong, K. Rhee, S. H. Kim, I. C. Kwon, K. Kim, *Adv. Funct. Mater.* **2013**, *23*, 5518.

[4] a) S. R. Sirsi, M. A. Borden, *Adv. Drug Delivery Rev.* **2014**, *72*, 3; b) A. V. Alexandrov, C. A. Molina, J. C. Grotta, Z. Garami, S. R. Ford, J. Alvarez-Sabin, J. Montaner, M. Saqqur, A. M. Demchuk, L. A. Moye, M. D. Hill, A. W. Wojner, F. Al-Senani, S. Burgin, S. Calleja, M. Campbell, C. I. Chen, O. Chernyshev, J. Choi, A. El-Mitwalli, R. Felberg, S. Ford, Z. Garami, W. Irr, J. Grotta, C. Hall, Y. Iguchi, J. Ireland, L. Labiche, M. Malkoff, L. Morgenstern, E. Noser, N. Okon, P. Piriyawat, D. Robinson, H. Shaltoni, S. Shaw, K. Uchino, F. Yatsu, J. Alvarez-Sabin, J. F. Arenillas, R. Huertas, C. Molina, J. Montaner, M. Ribo, M. Rubiera, E. Santamarina, M. Saqqur, N. Alchtar, F. O'Rourke, S. Hussain, A. Shuaib, E. Abdalla, A. Demchuk, K. Fischer, M. D. Hill, J. Kennedy, J. Roy, K. J. Ryckborst, M. Schebel, C. Investigators, *New Engl. J. Med.* **2004**, *351*, 2170.

[5] a) S. T. Kang, C. K. Yeh, *Chang Gung Med. J.* **2012**, *35*, 125; b) E. P. Stride, C. C. Coussios, *J. Eng. Med.* **2010**, *224*, 171.

[6] K. Tachibana, T. Uchida, K. Ogawa, N. Yamashita, K. Tamura, *Lancet* **1999**, *353*, 1409.

[7] a) O. D. Kripfgans, J. B. Fowlkes, D. L. Miller, O. P. Eldevik, P. L. Carson, *Ultrasound Med. Biol.* **2000**, *26*, 1177; b) M. L. Fabiilli, K. J. Haworth, I. E. Sebastian, O. D. Kripfgans, P. L. Carson, J. B. Fowlkes, *Ultrasound Med. Biol.* **2010**, *36*, 1364.

[8] N. Rapoport, K. H. Nam, R. Gupta, Z. Gao, P. Mohan, A. Payne, N. Todd, X. Liu, T. Kim, J. Shea, C. Scaife, D. L. Parker, E. K. Jeong, A. M. Kennedy, *J. Controlled Release* **2011**, *153*, 4.

[9] a) P. S. Sheeran, J. D. Rojas, C. Puett, J. Hjelmquist, C. B. Arena, P. A. Dayton, *Ultrasound Med. Biol.* **2015**, *41*, 814; b) T. Yin, P. Wang, R. Zheng, B. Zheng, D. Cheng, X. Zhang, X. Shuai, *Int. J. Nanomed.* **2012**, *7*, 895; c) Y. Zhou, Z. Wang, Y. Chen, H. Shen, Z. Luo, A. Li, Q. Wang, H. Ran, P. Li, W. Song, Z. Yang, H. Chen, Z. Wang, G. Lu, Y. Zheng, *Adv. Mater.* **2013**, *25*, 4123.

[10] a) P. Dayton, A. Klibanov, G. Brandenburger, K. Ferrara, *Ultrasound Med. Biol.* **1999**, *25*, 1195; b) Z. Gao, A. M. Kennedy, D. A. Christensen, N. Y. Rapoport, *Ultrasonics* **2008**, *48*, 260; c) R. Suzuki, T. Takizawa, Y. Negishi, K. Hagisawa, K. Tanaka, K. Sawamura, N. Utoguchi, T. Nishioka, K. Maruyama, *J. Controlled Rel.* **2007**, *117*, 130; d) C. H. Wang, S. T. Kang, C. K. Yeh, *Biomaterials* **2013**, *34*, 1852.

[11] a) M. Zhang, M. L. Fabiilli, K. J. Haworth, J. B. Fowlkes, O. D. Kripfgans, W. W. Roberts, K. A. Ives, P. L. Carson, *Ultrasound Med. Biol.* **2010**, *36*, 1691; b) E. Vlaisavljevich, Y. Y. Durmaz, A. Maxwell, M. Elsayed, Z. Xu, *Theranostics* **2013**, *3*, 851.

[12] N. Reznik, O. Shpak, E. C. Gelderblom, R. Williams, N. de Jong, M. Versluis, P. N. Burns, *Ultrasonics* **2013**, *53*, 1368.

[13] J. Y. Lee, K. H. Bae, J. S. Kim, Y. S. Nam, T. G. Park, *Biomaterials* **2011**, *32*, 8635.

[14] J. Zhuang, H. Wu, Y. Yang, Y. C. Cao, *J. Am. Chem. Soc.* **2007**, *129*, 14166.

[15] a) C. Antoine, *Comptes Rendus* **1888**, *107*, 681; b) P. S. Sheeran, S. Luois, P. A. Dayton, T. O. Matsunaga, *Langmuir* **2011**, *27*, 10412.

[16] N. Y. Rapoport, A. M. Kennedy, J. E. Shea, C. L. Scaife, K. H. Nam, *J. Controlled Release* **2009**, *138*, 268.

[17] S. Sirsi, M. Borden, *Bubble Sci. Eng. Technol.* **2009**, *1*, 3.

[18] Z. P. Du, M. P. Bilbao-Montoya, B. P. Binks, E. Dickinson, R. Ettelaie, B. S. Murray, *Langmuir* **2003**, *19*, 3106.

[19] N. W. Matsuura, R. Gorelikov, I. Chaudhuri, J. Rowlands, J. Hynynen, K. Foster, S. Burns, P. Resnik, Ultrasonics Symposium (IUS) 2009, IEEE International 2009, p. 5.

[20] O. Shpak, M. Verweij, H. J. Vos, N. de Jong, D. Lohse, M. Versluis, *Proc. Natl. Acad. Sci. USA* **2014**, *111*, 1697.

[21] a) D. Bardin, T. D. Martz, P. S. Sheeran, R. Shih, P. A. Dayton, A. P. Lee, *Lab Chip* **2011**, *11*, 3990; b) P. S. Sheeran, V. P. Wong, S. Luois, R. J. McFarland, W. D. Ross, S. Feingold, T. O. Matsunaga, P. A. Dayton, *Ultrasound Med. Biol.* **2011**, *37*, 1518.

[22] J. H. Park, G. Saravanakumar, K. Kim, I. C. Kwon, *Adv. Drug Delivery Rev.* **2010**, *62*, 28.

[23] J. D. Coffman, J. A. Lempert, *Circulation* **1975**, *52*, 141.

[24] D. Carugo, J. Owen, C. Crake, J. Y. Lee, E. Stride, *Ultrasound Med. Biol.* **2015**, *41*, 1927.

[25] a) P. A. Dijkmans, L. J. Juffermans, R. J. Musters, A. van Wamel, F. J. ten Cate, W. van Gilst, C. A. Visser, N. de Jong, O. Kamp, *Eur. J. Echocardiogr.* **2004**, *5*, 245; b) M. M. Kaneda, S. Caruthers, G. M. Lanza, S. A. Wickline, *Ann. Biomed. Eng.* **2009**, *37*, 1922.

[26] C. H. Wang, S. T. Kang, Y. H. Lee, Y. L. Luo, Y. F. Huang, C. K. Yeh, *Biomaterials* **2012**, *33*, 1939.

[27] B. Krasovitski, V. Frenkel, S. Shoham, E. Kimmel, *Proc. Natl. Acad. Sci. USA* **2011**, *108*, 3258.

[28] C. Crake, M. de Saint Victor, J. Owen, C. Coviello, J. Collin, C. C. Coussios, E. Stride, *Phys. Med. Biol.* **2015**, *60*, 785.

[29] T. G. Leighton, *The Acoustic Bubble*, Academic Press, London **1994**.

[30] L. A. Edwards, B. Thiessen, W. H. Dragowska, T. Daynard, M. B. Bally, S. Dedhar, *Oncogene* **2005**, *24*, 3596.

[31] R. C. Taylor, S. P. Cullen, S. J. Martin, *Nat. Rev. Mol. Cell Biol.* **2008**, *9*, 231.

[32] a) J. Y. Lee, J. H. Kim, K. H. Bae, M. H. Oh, Y. Kim, J. S. Kim, T. G. Park, K. Park, J. H. Lee, Y. S. Nam, *Small* **2015**, *11*, 222; b) P. B. Schiff, J. Fant, S. B. Horwitz, *Nature* **1979**, *277*, 665.

COMMUNICATION